# Modelling the viral dynamics of the SARS-CoV-2 Delta and Omicron variants in different cell types

Clare P. McCormack[1]*, Ada W. C. Yan[2]*, Jonathan C. Brown[2], Ksenia Sukhova[2], Thomas P. Peacock[2], Wendy S. Barclay[2], Ilaria Dorigatti[1]

[1]MRC Centre for Global Infectious Disease Analysis, School of Public Health, Imperial College London, London, United Kingdom

[2]Department of Infectious Disease, Imperial College London, London, United Kingdom

*contributed equally, joint corresponding authors

## Abstract

We use viral kinetic models fitted to viral load data from *in vitro* studies to explain why the SARS-CoV-2 Omicron variant replicates faster than the Delta variant in nasal cells, but slower than Delta in lung cells, which could explain Omicron's higher transmission potential and lower severity. We find that in both nasal and lung cells, viral infectivity is higher for Omicron but the virus production rate is higher for Delta. However, the differences are unequal between cell types, and ultimately leads to the basic reproduction number and growth rate being higher for Omicron in nasal cells, and higher for Delta in lung cells. In nasal cells, Omicron alone can enter via a TMPRSS2-independent pathway, but it is primarily increased efficiency of TMPRSS2-dependent entry which accounts for Omicron's increased activity. This work paves the way for using within-host mathematical models to understand the transmission potential and severity of future variants.

41 ## Introduction

42 Since its designation as a variant of concern (VOC) by the World Health Organization on 26th November
43 2021[1], the Omicron (B.1.1.529\BA.1) variant of severe acute respiratory coronavirus 2 (SARS-CoV-2)
44 has rapidly displaced the Delta (B.1.617.2) variant to become the dominant SARS-CoV-2 variant
45 globally[2–4]. Analyses have demonstrated that Omicron can partially evade the immunity generated
46 through previous infection and vaccination[5–8], thereby leading to reduced vaccine effectiveness
47 against symptomatic disease[9].

48 Despite this reduction in vaccine effectiveness against symptomatic disease, the risk of severe
49 outcomes (including hospital admission and death) following infection with Omicron is substantially
50 lower than following infection with Delta, for both vaccinated and unvaccinated individuals[10,11]. While
51 much remains to be understood about the mechanisms underpinning this observation, a reduction in
52 the capacity of Omicron relative to Delta to replicate in lung cells has been suggested as a possible
53 explanation[12]. On the other hand, Omicron's increased ability to replicate in nasal cells has been
54 suggested as an explanation for Omicron's transmission advantage over Delta observed from
55 epidemiological data[13–15].

56 It has been hypothesised that these differences in viral replication capacity in different cells can be
57 attributed to how Omicron and Delta utilise different pathways to enter host cells[12,16–18]. All SARS-CoV-
58 2 viruses can enter cells which express both ACE2 and TMPRSS2 proteins, via fusion of the viral and
59 cell membranes or via early endosomes[19]. However, Omicron is also able to efficiently enter ACE2+
60 cells via fusion from the endosome after endocytosis, without the involvement of TMPRSS2[16,20]. This
61 could expand the range of cells that Omicron can infect. A complication is by entering cells via the
62 endosome, SARS-CoV-2 may be inhibited by endosomal restriction factors such as interferon-induced
63 IFITM proteins[21,22] or NCOA7[23]. Understanding how virological properties shape the viral dynamics of
64 SARS-CoV-2 in different cell types can enhance our understanding of the mechanisms underlying the
65 observed differences in transmissibility between the Omicron and Delta variants. The different entry
66 pathways and their inhibition by endosomal restriction factors are shown in Figure 1.

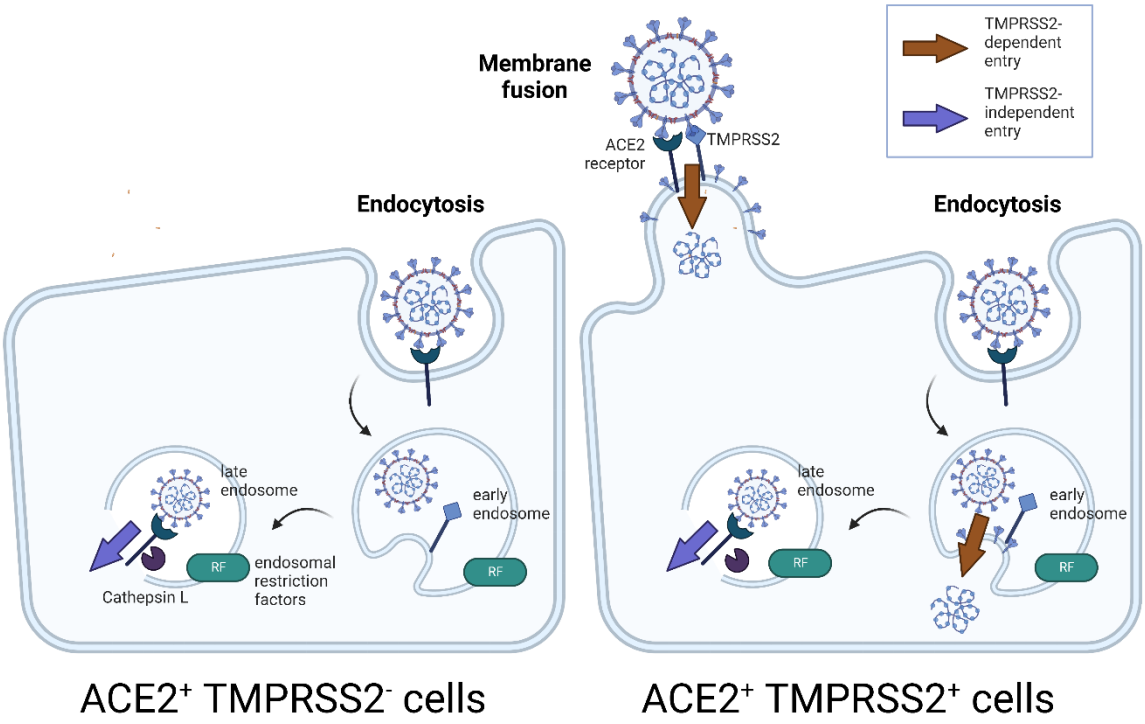


**Figure 1. Illustration of TMPRSS2-dependent and TMPRSS2-independent entry pathways and their inhibition by endosomal restriction factors**. In ACE2+ TMPRSS2+ cells (right), virus can enter in a TMPRSS2-dependent way via membrane fusion either at the cell surface or the early endosome; alternatively, virus can enter in a TMPRSS2-independent way through the late endosome. In ACE2+ TMPRSS2- cells (left), only the TMPRSS2-independent pathway is available. Both pathways can be inhibited by endosomal restriction factors. Created with BioRender.com.

Mechanistic mathematical models, calibrated against virological data, are a powerful tool for exploring viral dynamics as they provide a framework to quantify key characteristics of different variants and build an understanding of the drivers of inter-individual variation in response to infection. For example, previous within-host modelling studies of SARS-CoV-2 have enabled an understanding of the effect of covariates such as age, sex, and disease severity on viral load[24], the degree of heterogeneity between individuals[25], and the potential effect of antivirals and masking on viral load[26–30]. Models fitted to data from vaccine trials have suggested correlates of protection[31], while more theoretical immunological models have also been developed with the ultimate aim of understanding the interplay between the immune response and disease severity[32–34]. Studies linking the within- and between-host scales have improved the understanding of the relationship between Ct values and infectiousness[25,35], suggested characteristics of optimal testing regimes[36] and provided explanations for population-level epidemiological observations, e.g. the apparent reduction in viral load observed during the declining phase of an epidemic[37].

The studies mentioned above have all fitted their models to data from *in vivo* studies. While dynamics in humans are of ultimate interest, modelling viral kinetics and the immune response *in vivo* is

extremely complex. Moreover, studies in humans are often limited, with little or no information on the timing and amount of the viral inoculum, sparse longitudinal observations, and often no available measurements before the start of symptom onset[25,35]. *In vitro* studies offer a simplification of *in vivo* dynamics, where both the inoculum and method of inoculation is controlled, and where some components of the immune response – such as the adaptive immune response – are eliminated. Viral load can be measured from the start of infection, which is important for estimating the growth rate and basic reproduction number of the virus, which in turn can be used to assess the potential for load variants to outcompete existing variants.

Here, using viral kinetics models calibrated against viral replication data generated through experimental infection studies in primary human nasal epithelial cells (hNECs) and immortalised Calu-3 lung cells, we characterise and compare the dynamics of Omicron and Delta viruses in each cell type by quantifying key properties such as the basic reproduction number and growth rate, and by exploring how these properties vary for different entry pathways, and in the presence and absence of functional endosomal restriction factors.

# Methods

**Experimental Design/Data**

Full details of the viral kinetics experiments conducted are provided in Peacock et al.[20] . In brief, Calu-3 and primary human nasal epithelial cells (hNECs) were inoculated with Omicron BA.1 and Delta/B.1.617.2 isolates at an MOI of 0.001 (Calu-3) or 0.05 (hNECs), and incubated for 1 hr at 37°C. The inoculum was then removed and, in the case of Calu-3 cells, replaced with 1 mL serum-free DMEM. For Calu-3 cells, 100 µL of supernatant was collected for titration at 18, 24, 48 and 72 hours post-infection. For hNECs, at the same timepoints post-infection, the supernatant was collected by adding 200 µL of serum-free DMEM to the apical surface, incubating for 10 minutes, and removing for collection.

Additional experiments were performed to investigate the effect of Camostat mesylate (henceforth referred to as Camostat) and Amphotericin B on viral kinetics. Camostat is a serine protease inhibitor and thus inhibits TMPRSS2, while Amphotericin B inhibits the restriction of viral endosomal entry by endosomal restriction factors such as IFITM proteins[38–40]. Cells were pre-treated both basolaterally and apically with either 50 µM of Camostat, 1µM of Amphotericin B or no drug for 2 hours prior to infection, and this concentration of drug was maintained in the basolateral media throughout the experiment. Infections and collection of timepoints were performed as above.

120 All experiments were performed in triplicate. Infectious viral titres were quantified by plaque assay
121 and viral genome numbers were quantified by E gene RT-qPCR.

122 **Mathematical Models**

123 *Model 1*

124 To gain an initial understanding of the differences between the observed infection dynamics of the
125 Omicron and Delta variants across each cell type, we first developed a simple model of the viral
126 dynamics which assumed a single virus entry pathway for both variants. A simple schematic of the
127 model is provided in Figure 2. Model equations are in the Supplementary Methods.

128 Target cells $T$ become infected at a rate $\beta$ (target cell infection rate) per infectious virion ($V_{Inf}$). The
129 target cell infection rate is defined as the proportion of cells infected per day, per unit inoculum of 1
130 pfu/mL. Following an eclipse phase of mean duration of $1/\tau$ days, infectious cells (I) produce infectious
131 and non-infectious virus. Infectious virus ($V_{Inf}$), as measured by plaque-assay, and total (infectious and
132 non-infectious) virus ($V_{RNA}$), as measured by RT-qPCR, are produced at rates $\omega_{\mathrm{Inf}}$ and $\omega_{\mathrm{RNA}}$
133 respectively. (While the RT-qPCR assay could detect viral RNA released from lysed cells as well as from
134 extracellular viral particles, the model assumes that all detected viral RNA originates from viral
135 particles.) The duration of the eclipse phase $1/\tau$ reflects the speed of a single viral replication cycle,
136 whereas the rate of viral production $\omega_{Inf}$ also reflects replication capacity. Infectious cells have a
137 mean lifespan of $1/\delta$ days, and infectious and non-infectious virus is assumed to decay at rates $\kappa_{\mathrm{Inf}}$
138 and $\kappa_{\mathrm{RNA}}$ respectively, with additional loss due to entry into cells. Cells which express the ACE2
139 receptor, which is required for SARS-CoV-2 virus entry, are considered target cells.

140

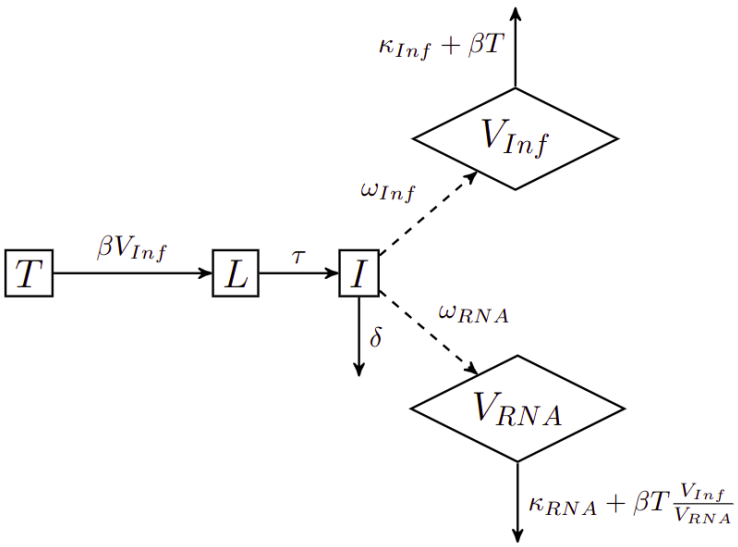


**Figure 2: Compartmental diagram of model 1**. Target cells $T$ become infected at a rate $\beta$ per infectious virion ($V_{Inf}$). Following an eclipse phase of mean duration of $1/\tau$ days, infectious cells (I) produce infectious virus as measured by plaque-assay ($V_{Inf}$) and total virus as measured by qPCR ($V_{RNA}$) at rates $\omega_{Inf}$ and $\omega_{RNA}$ respectively. Infected cells have a mean lifespan of $1/\delta$ days, and infectious and total virus are assumed to decay at rates $\kappa_{Inf}$ and $\kappa_{RNA}$ respectively.

*Model 2*

The experimental data showed that while Delta can only enter ACE2$^+$ cells by utilizing the TMPRSS2 protein, Omicron can enter these cells both through TMPRSS2- dependent and TMPRSS2-independent pathways. Thus, in Model 2 we modify Model 1 to account for the two possible cell entry pathways, where TMPRSS2-independent pathways can be used to infect all ACE2$^+$ cells, and TMPRSS2-dependent pathways can only infect ACE2$^+$ TMPRSS2$^+$ cells. We assume that all ACE2$^+$ cells become infected through TMPRSS2-independent pathways at a rate $\beta_E$ per infectious virion ($V_{Inf}$) and that ACE2$^+$ TMPRSS2$^+$ target cells ($T_+$) also become infected through TMPRSS2-dependent pathways at a rate $\beta_T$ per infectious virion. We assume that endosomal restriction factors decrease the infectivity through the TMPRSS2-independent pathways by a factor $f_E$, and through TMPRSS2-dependent pathways by a factor $f_T$. Cells infected through TMPRSS2-independent and TMPRSS2-dependent pathways ($L_E$ and $L_T$ respectively) undergo eclipse phases of mean duration $1/\tau_E$ and $1/\tau_T$ days respectively. Following the eclipse phase, infectious cells (I) behave as per Model 1. The flow diagram of Model 2 is described in Figure 3.

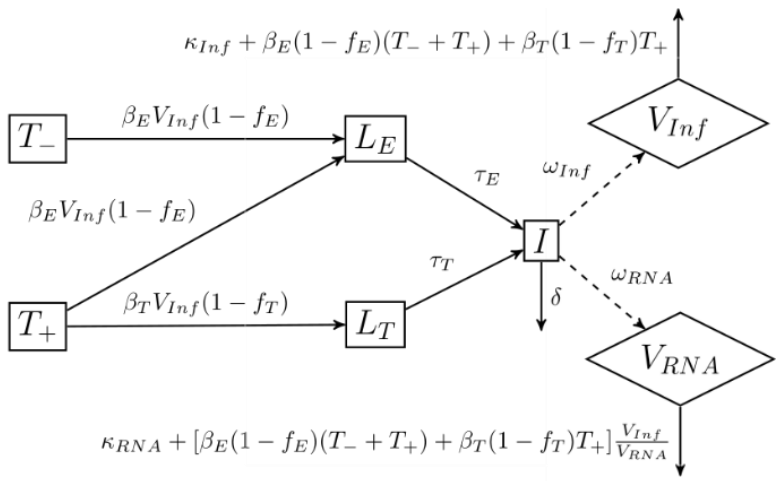


**Figure 3: Compartmental diagram for Model 2**. ACE2⁺ TMPRSS2⁻ target cells ($T_-$) become infected through TMPRSS2-independent pathways at a rate $\beta_E$ per infectious virion ($V_{Inf}$). ACE2⁺ TMPRSS2⁺ target cells ($T_+$) become infected through TMPRSS2-independent pathways at a rate $\beta_E$ per infectious virion, and through TMPRSS2 -dependent pathways at a rate $\beta_T$ per infectious virion. Endosomal restriction factors decrease the infectivity through TMPRSS2-independent pathways by a factor $f_E$, and through TMPRSS2-dependent pathways by a factor $f_T$. Cells infected through TMPRSS2-independent and TMPRSS2-dependent pathways ($L_E$ and $L_T$ respectively) undergo eclipse phases of mean duration $1/\tau_E$ and $1/\tau_T$ days respectively. Following the eclipse phase, infectious cells (I) behave as per Model 1.

Model 2 is fitted to hNEC and Calu-3 data without drug, in the presence of Camostat, in the presence of Amphotericin B, and in the presence of both drugs. For each virus strain/cell type combination, all data (with and without drugs) is fitted simultaneously. Camostat is assumed to completely inhibit TMPRSS2-dependent pathways (we set $\beta_T = 0$); although Camostat also inhibits other serine proteases, but as TMPRSS2 is the main serine protease involved in SARS-CoV-2 virus entry, and because the activation of S2' in TMPRSS2-independent pathways likely occurs by cathepsin proteases rather than serine proteases, for simplicity we assume that Camostat does not affect TMPRSS2-independent pathways. Amphotericin B is assumed to completely remove endosomal restriction (we set $f_E = f_T = 0$).

*Inferential framework*

We calibrated the models to the observed data in a Bayesian inferential framework using Markov Chain Monte Carlo (MCMC) methods. In the results, we reported the median and 95% credible interval (CrI) of the parameter estimates. Full details of the model fitting algorithms are provided in the Supplementary Methods.

# Results

**<u>Data Description</u>**

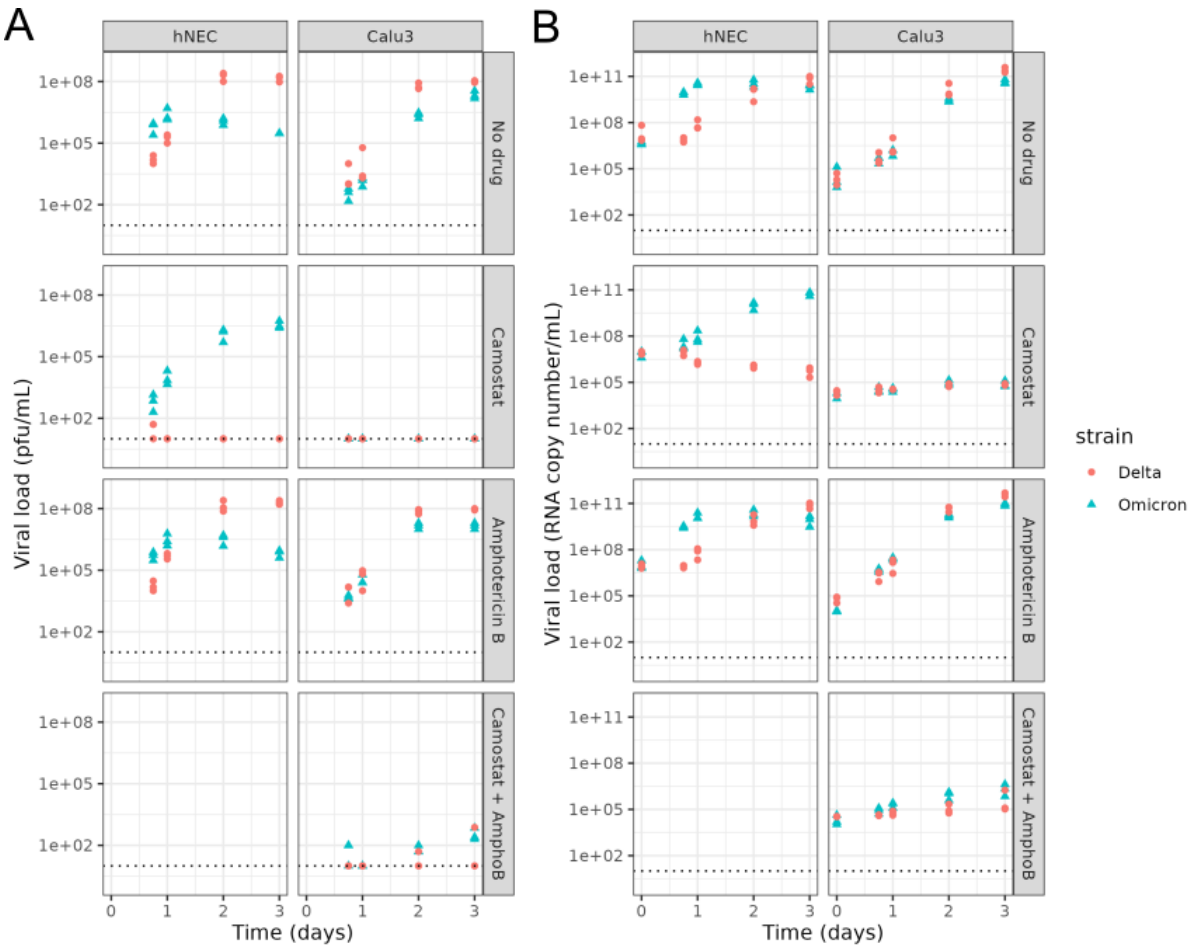


**Figure 4: Summary of Data.** (A) Infectious viral load (pfu/mL) quantified by plaque assay and (B) RNA copy number/mL quantified by RT-qPCR for Omicron (blue triangles) and Delta (red dots) for different cell types (columns) and drug treatments (rows). The dotted line shows the limit of detection; markers on the lines represent measurements below the limit of detection. Cells were infected on day 0.

Figure 4 summarises the study data. In control wells with no drug, temporal trends in viral growth varied both between strains and cell type. In hNECs, Omicron grew more rapidly than Delta, with viral load peaking by 1 day post infection (p.i.) for Omicron, compared with 2 days p.i. for Delta. However, despite this initial growth advantage, viral load was higher for Delta compared to Omicron at 3 days p.i.. In Calu-3 cells, the peak in viral load was observed 2-3 days p.i. for both Omicron and Delta. In contrast with hNECs where the strain corresponding to the highest viral load was dependent on measurement time, infectious and non-infectious viral load was higher for Delta than Omicron across all time points for Calu-3 cells.

In the presence of the drug Camostat which inhibits serine proteases, and thus TMPRSS2-dependent pathways, replication of Delta was severely inhibited in hNECs with no detectable increase in virus throughout the course of the experiment. In contrast, Omicron successfully replicated in hNECs in the presence of Camostat, albeit at a slower rate than in untreated wells. However, similar levels of viral

209 load were obtained by 2-3 days p.i. in both the presence and absence of Camostat. For both strains,
210 the presence of Amphotericin B had little impact on viral load dynamics in hNECs. In Calu-3 cells,
211 infectious virus was not detected at any point for either Omicron or Delta in the presence of Camostat.
212 In the presence of the drug Amphotericin B which is described as specifically inhibiting endosomal
213 restriction[22,39], Omicron infectious viral titres were consistently higher than in control wells, until 3
214 days p.i. when titres became similar. Delta geometric mean infectious viral titres were similar with
215 and without Amphotericin B.
216
217 Experiments with both drugs combined were only performed for Calu-3 cells. For both virus strains,
218 the infectious viral load was below the limit of detection in the presence of Camostat only. Adding
219 Amphotericin B raised the infectious viral load to above the limit of detection for all replicates for
220 Omicron, but only for some replicates for Delta (Figure 4).
221
222 **Viral Fitness**
223
224 **Model 1**

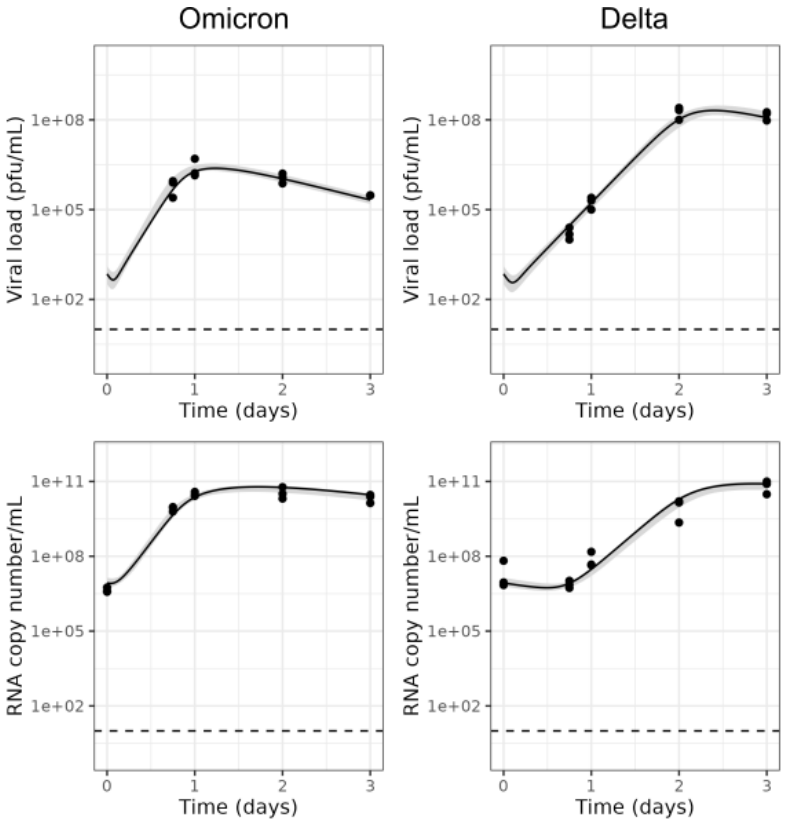


225

226 **Figure 5: Model 1 fits to data from hNECs without drugs.** Dots show the data, black lines show the maximum likelihood
227 fit, shaded areas show the 95% credible interval (CrI) and dotted lines show the limit of detection.

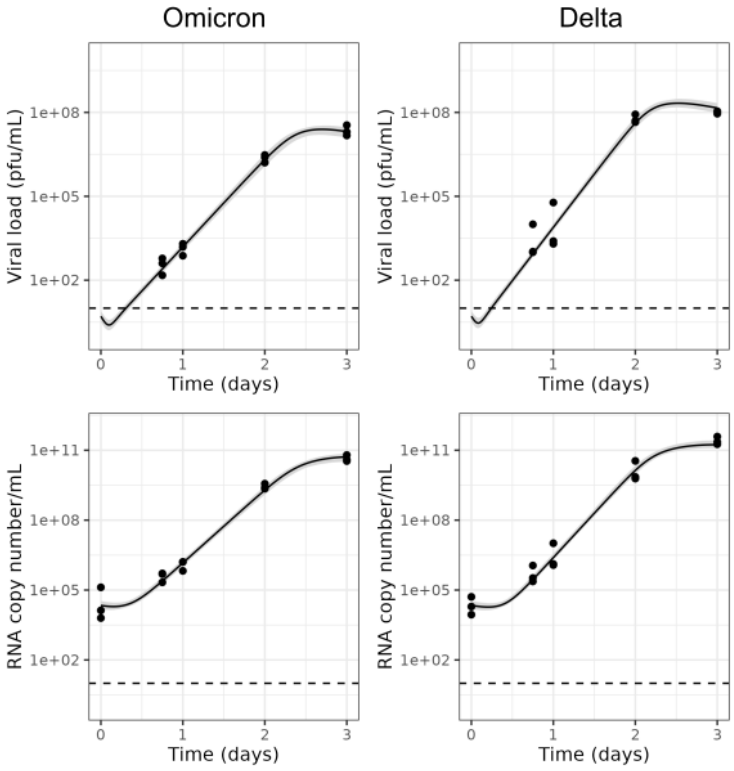


**Figure 6: Model 1 fits to data from Calu-3 cells without drugs**. Dots show the data, black lines show the maximum likelihood fit, shaded areas show the 95% credible interval (CrI) and dotted lines show the limit of detection.

For both Omicron and Delta, the simple model (Model 1) captured the viral dynamics observed in control wells of hNECs and Calu-3 cells (Figures 5, 6). For hNECs, we estimated a higher target cell infection rate $\beta$ for Omicron relative to Delta (2.13e-05 (95% CrI: 1.54e-05, 3.07e-05) cell (pfu/mL)$^{-1}$ day$^{-1}$ for Omicron, 8.89e-08 (95% CrI: 5.91e-08, 1.28e-07) cell (pfu/mL)$^{-1}$ day$^{-1}$ for Delta), but a lower infectious virus production rate $\omega_{Inf}$ for Omicron relative to Delta (4.07e+03 (95% CrI: 3.13e+03, 5.50e+03) pfu/mL cell$^{-1}$ day$^{-1}$ for Omicron, 3.42e+05 (95% CrI: 2.41e+05, 5.04e+04) pfu/mL cell$^{-1}$ day$^{-1}$ for Delta). All estimated parameters are presented in Supplementary Table 2. These results suggest an approximately 1.5-fold difference in the growth rate between these strains in hNECs, with a growth rate of 11.61 day$^{-1}$ (95% CrI: 10.43,12.99) for Omicron and 6.87 day$^{-1}$ (95% CrI: 6.33,7.50) for Delta. Furthermore, we estimated a higher basic reproduction number ($R_0$) for Omicron (65.04 (95% CrI: 51.94, 82.71)) compared with Delta (23.13 (95% CrI: 19.91, 27.23)), thereby suggesting an overall increase in viral fitness of Omicron relative to Delta in hNECs.

For Calu-3 cells, we estimated a higher target cell infection rate for Omicron than Delta (9.23e-07 (95% CrI: 6.17e-07, 1.36e-06) cell (pfu/mL)$^{-1}$ day$^{-1}$ for Omicron, 1.42e-07 (95% CrI: 9.80e-08, 2.05e-07) cell

247 (pfu/mL)$^{-1}$ day$^{-1}$ for Delta) and lower infectious virus production rate for Omicron than Delta (4.13e+02
248 (95% CrI: 2.85e+02,6.07e+02) cell (pfu/mL)$^{-1}$ day$^{-1}$ for Omicron, 3.73e+03 (95% CrI:
249 2.67e+03,5.32e+03) cell (pfu/mL)$^{-1}$ day$^{-1}$ for Delta). In contrast with hNECs, our results indicate an
250 overall increase in viral fitness of Delta relative to Omicron in Calu-3 cells as we estimated a higher
251 basic reproduction number of Delta (36.67 (95% CrI: 33.69, 39.81)) compared to Omicron (24.23 (95%
252 CrI: 22.14, 26.70)) in this cell type. In addition, we estimated a larger growth rate of Delta relative to
253 Omicron in Calu-3 cells, with a growth rate of 8.78 day$^{-1}$ (95% CrI: 8.40, 9.15) for Delta compared with
254 7.25 day$^{-1}$ (95% CrI: 6.86, 7.60) for Omicron (for details see Supplementary Table 2).

255

256 For both cell types, the target cell infection rate ($\beta$), which is positively correlated with the probability
257 of a virion successfully infecting a cell, was higher for Omicron than Delta. The infectious virus
258 production rate ($\omega_{Inf}$), which is directly proportional to the burst size (the total number of infectious
259 virions produced by one infected cell), was higher for Delta than Omicron. However, the magnitude
260 of each of these differences meant that the basic reproduction number and growth rate, which are
261 both functions of the target cell infection rate and the infectious virus production rate (see
262 Supplementary Methods), were higher for Omicron in hNECs, but higher for Delta in Calu-3 cells
263 (Supplementary Table 2).

264

265 **Model 2**

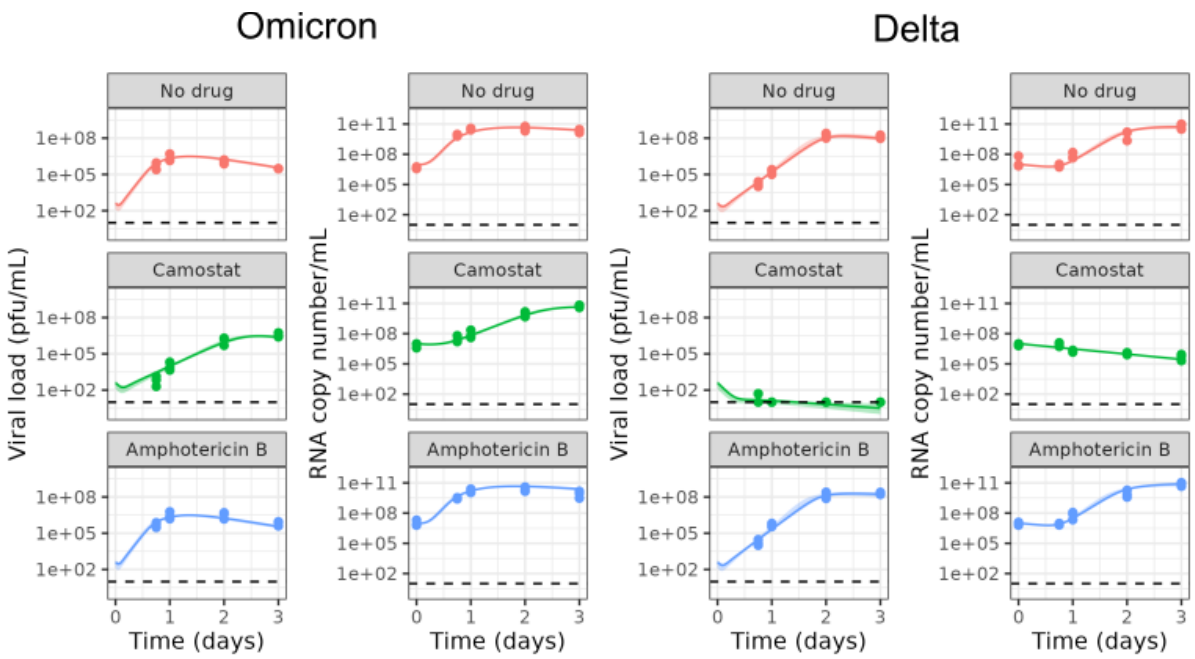


266

**Figure 7. Model 2 fits to data from hNECs with and without drugs.** Dots show the data, black lines show the maximum likelihood fit, shaded areas show the 95% credible interval (CrI) and dotted lines show the limit of detection. Markers on the lines represent measurements below the limit of detection.

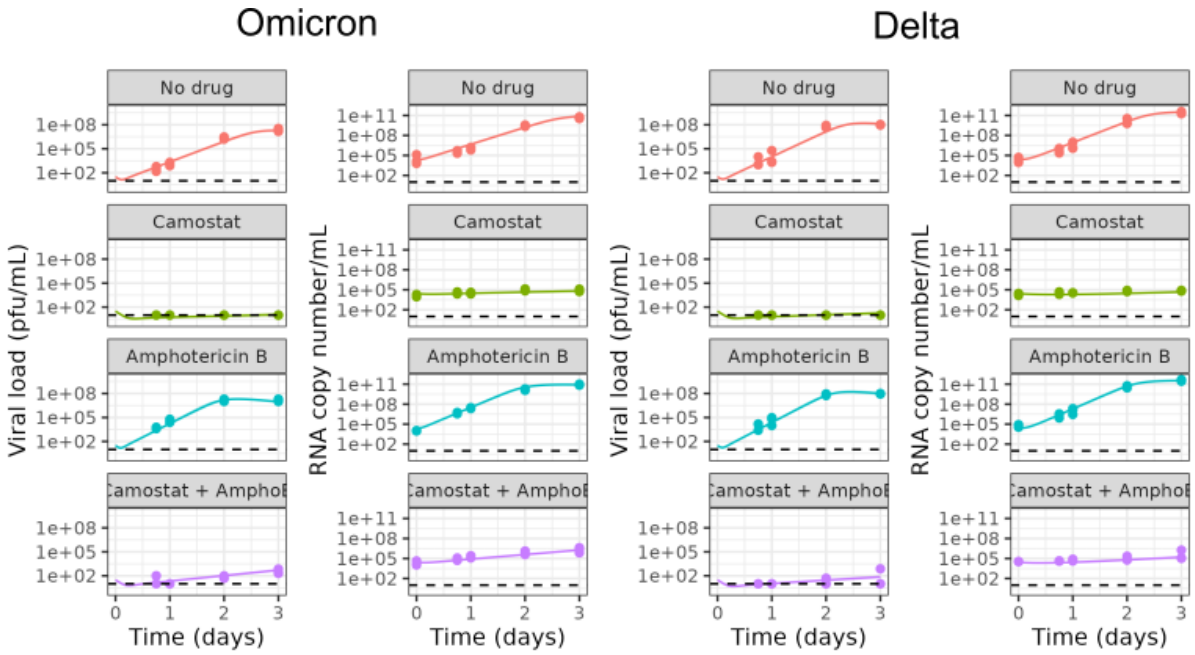


**Figure 8. Model 2 fits to data from Calu-3 cells with and without drugs**. Dots show the data, black lines show the maximum likelihood fit, shaded areas show the 95% credible interval (CrI) and dotted lines show the limit of detection. Markers on the lines represent measurements below the limit of detection.

When fitting Model 2 to the data, we found the same qualitative result that Omicron's $R_0$ is higher than Delta's in hNECs, but lower in Calu-3 cells (Figures 7 and 8). In hNECs, $R_0$ for Omicron was estimated to be 94.35 (95% CrI: 75.32, 119.85), while for Delta it was estimated to be 29.95 (95% CrI: 24.20, 38.38). In Calu-3 cells, $R_0$ for Omicron was estimated to be 17.21 (95% CrI: 16.03, 18.53), and for Delta was estimated to be 26.02 (95% CrI: 24.48, 27.99). $R_0$ estimates were comparable between Models 1 and 2, except for Omicron in hNECs, where the $R_0$ estimates obtained with Model 2 were higher. This discrepancy occurred because Model 2 predicts that Omicron can use both TMPRSS2-dependent and TMPRSS2-independent pathways in hNECs (see next section), whereas for all other strain and cell combinations only TMPRSS2-dependent pathways are active. When only TMPRSS2-dependent pathways are active, then in the absence of drug, Models 1 and Model 2 are the same. All parameter estimates are presented in Supplementary Table 1.

## Role of Cell Entry Pathways

As Camostat inhibits serine proteases including TMPRSS2, Camostat-sensitive viruses must be able to use TMPRSS2-independent pathways for cell entry; thus, the fit of Model 2 to the data in the presence of Camostat provides information on the role of cell entry pathways. We found that in hNECs, Omicron

292 was able to utilise both TMPRSS2-dependent and TMPRSS2-independent pathways. The median
293 estimates of $R_{0T}$ and $R_{0E}$ were 81.71 (95% CrI: 63.72, 104.73) and 13.44 (95% CrI 11.17, 16.62)
294 respectively (Supplementary Table 3). On the other hand, in hNECs, Delta was unable to effectively
295 use TMPRSS2-independent pathways, as $R_{0E} < 1$ (median 0.49, 95% CrI: (0.24, 0.82)). In Calu-3s,
296 neither virus was able to use TMPRRS2-independent pathways effectively. $R_{0E}$ was estimated to be
297 slightly greater than 1 for both Omicron (median 1.42 (95% CrI: 1.24, 1.62)) and Delta (median 1.56
298 (95% CrI: 1.36, 1.77)) but these small values of $R_0$ are insufficient for the viral load to exceed the limit
299 of detection during the time course of the experiment (Figure 8 Camostat panels). Note that for
300 Omicron in hNECs, the estimate for $R_{0T}$ is comparable to the overall $R_0$ for Model 1. This is because
301 the increase in viral load due to TMPRSS2-dependent pathways is much faster than through TMPRSS2-
302 independent pathway, so the TMPRSS2-dependent pathway is the main contributor to the initial
303 exponential increase, from which Model 1 estimates $R_0$.
304
305 It has been suggested that Omicron's use of TMPRRS2-independent pathways explains its fitness
306 advantage over Delta[12,16,17]. However, even the TMPRSS2-specific basic reproduction number is higher
307 for Omicron than Delta in hNECs, with a median $R_{0T}$ equal to 81.71 (95% CrI: 63.72, 104.73) for
308 Omicron compared to 29.46 (95% CrI: 23.98, 37.72) for Delta. In fact, $R_{0T}$ alone for Omicron is greater
309 than the overall $R_0$ for Delta. Therefore, it is primarily Omicron's more efficient use of TMPRSS2-
310 dependent pathways, rather than its utilisation of TMPRSS2-independent pathways, which gives it a
311 fitness advantage over Delta in hNECs.
312
313 **Role of endosomal restriction**
314
315 As Amphotericin B inhibits restrictions to virus entry imposed by endosomal restriction factors, the fit
316 of Model 2 to the Amphotericin B data provides information on the role of endosomal restriction
317 factors in shaping the viral dynamics observed. The parameters $f_E$ and $f_T$ capture the degree of
318 inhibition of TMPRSS2-independent and TMPRSS2-dependent pathways by endosomal restriction
319 factors respectively, and Amphotericin B is assumed to set these parameters to 0. Comparing across
320 cell types, inhibition by endosomal restriction factors was higher in Calu-3 cells than hNECs across all
321 strains and pathways (higher values of $f_E$ and $f_T$ for Calu-3 cells compared to hNEC cells in
322 Supplementary Table 4), with the exception of TMPRSS2-independent pathways for Delta, where $f_E$
323 could not be estimated precisely. Inhibition was similar for both Omicron and Delta in hNECs, but
324 Omicron was more inhibited by endosomal restriction factors than Delta in Calu-3 cells for both
325 pathways (higher values of $f_E$ and $f_T$ for Omicron than Delta in Calu-3 cells in Supplementary Table

326 4). Comparing across pathways, $f_E$ and $f_T$ were similar for each virus strain in hNECs, but in Calu-3
327 cells, $f_E$ was higher than $f_T$ for both virus strains, suggesting more inhibition of TMPRSS2-independent
328 pathways than of TMPRSS2-dependent pathways.
329
330 Given that TMPRSS2-independent pathways are susceptible to inhibition by endosomal restriction
331 factors, and that previous variants were not able to use endosomal restriction pathways, one may
332 hypothesise that Omicron has overcome endosomal restriction in hNECs, and that TMPRSS2-
333 independent pathways would also be accessible by other virus-cell combinations if endosomal
334 restriction were lifted. However, we predict that even if endosomal restriction is lifted for the three
335 other virus-cell combinations (as per the Amphotericin B experiments) $R_{0EX}$ remains low. This
336 suggests that other factors contribute to Omicron's increased use of TMPRSS2-independent pathways
337 in hNECs. We predict that in the absence of endosomal restriction factors, Omicron would still have a
338 higher overall basic reproduction number and growth rate than Delta in hNECs, but these quantities
339 would be similar between variants in Calu-3 cells ($R_{0X}$ in Supplementary Table 3 and $r_X$ in
340 Supplementary Table 6).
341
342 **Changing the assumed eclipse phase duration**
343
344 A caveat of the above results is that we have fixed the length of the eclipse phase. The eclipse phase
345 in this model reflects the speed of viral replication with the cell. To date, studies which have measured
346 the duration of the eclipse phase in the SARS-CoV-2 viral life cycle have used viruses which enter target
347 cells through TMPRSS2-dependent pathways only[41,42]. Thus, the duration of the eclipse phase for
348 TMPRSS2-independent pathways is unclear and our knowledge of this component of the viral life cycle
349 is limited. To address this, we conducted a sensitivity analysis around the duration of the eclipse phase.
350 In Model 1, $\tau$ was set to 6, 4, or 2 day$^{-1}$. In Model 2, $\tau_T$ was set to 6, 4 or 2 day$^{-1}$, and $\tau_E$ was set to 4,
351 2 or 1 day$^{-1}$. We found that for Model 1, regardless of the duration of the eclipse phase assumed – as
352 long as it was the same between strains – Omicron had a higher $R_0$ than Delta in hNECs, and Delta
353 had a higher $R_0$ than Omicron in Calu-3 cells (Supplementary Table 4). Also, all estimated $R_0$ values
354 decreased as the duration of the eclipse phase decreased, as expected theoretically. This is because
355 if, at the start of infection, cells start producing virus sooner due to a short eclipse phase, then each
356 individual infected cell needs to lead to fewer secondary infections to reproduce the dynamics
357 observed. Similarly, for Model 2, we found that regardless of the values of $\tau_E$ and $\tau_T$, as long as these
358 were assumed to be the same between strains, Omicron had a higher $R_0$ than Delta in hNECs, and
359 Delta had a higher $R_0$ than Omicron in Calu-3 cells; only Omicron in hNECs used TMPRSS2-independent

pathways efficiently; and endosomal restriction only had a significant effect in Calu-3 cells (Supplementary Table 5). However, allowing the duration of the eclipse phase to be different between strains, no longer allows us to draw conclusions about whether $R_0$ is greater for Omicron or Delta (Supplementary Tables 3 and 5). On the other hand, estimates of the growth rate *r* only varied slightly with the assumed duration of the eclipse phase for both models (Supplementary Tables 4 and 6).

367 ## Discussion

368 By fitting a simple within-host model to viral kinetics data for Omicron and Delta in hNECs and Calu-3
369 cells we found that Omicron has a fitness advantage over Delta in hNECs, but Delta has a fitness
370 advantage over Omicron in Calu-3 cells, as measured by both the growth rate and basic reproduction
371 number of the virus. These findings are consistent with previously published studies showing faster
372 replication of Omicron compared with Delta in human nasal epithelial cells[14,16], and faster replication
373 of Delta compared with Omicron in the ex vivo explant cultures of human lungs[12] and Calu-3 cells[43].

374 We estimated that Omicron had a higher rate of infection $\beta$ in both cell types, which could be linked
375 to increased ACE2 binding affinity, likely due to mutations in the spike protein. Evidence is mixed as
376 to whether Omicron has a higher ACE2 binding affinity than Delta. Cameroni et al.[44] found that
377 Omicron has a higher human ACE2 binding affinity than Delta, but Mannar et al.[45] found that ACE2
378 binding affinity is similar for Omicron and Delta, though higher than the ancestral strain. On the other
379 hand, Zhang et al.[46] found that the Omicron spike protein required a higher level of ACE2 than Delta
380 for efficient membrane fusion. We also estimated that Omicron had a lower rate of infectious virus
381 production $\omega_{Inf}$ than Delta for both cell types. Changes to the rate of viral production could be due
382 to mutations in either spike or non-spike proteins. The basic reproduction number is positively
383 correlated with both the rate of infection $\beta$ and the rate of infectious virus production $\omega_{Inf}$ in our
384 models. In hNECs, the increase in the rate of infection $\beta$ for Omicron was greater than the decrease
385 in infectious virus production $\omega_{Inf}$, resulting in a larger basic reproduction number and growth rate
386 for Omicron compared to Delta; the converse was true in Calu-3 cells.

387 Previous studies have proposed that TMPRSS2-independent pathways which are only available to
388 Omicron are responsible for its faster growth in hNECs. Our study found that Omicron can use
389 TMPRSS2-independent pathways in hNECs, consistent with the previous studies. However, the
390 growth rate and basic reproduction number for TMPRSS2-independent pathways was low and
391 insufficient to explain the overall fitness advantage for Omicron over Delta in hNECs. On the other
392 hand, the growth rate and basic reproduction number for TMPRSS2-dependent pathways was also
393 higher for Omicron than Delta in hNECs and was sufficient to explain the overall fitness advantage.
394 Evidence for the continued importance of TMPRSS2-dependent pathways for Omicron was provided
395 by a study by Metzdorf et al.[47] which found that the growth of Omicron in the nose and lung was
396 attenuated in TMPRSS2 knockout mice. In Calu-3 cells, neither Omicron nor Delta can use TMPRSS2-
397 independent pathways, thereby providing further insight into how these viruses use different
398 pathways to enter target cells.

399 We estimated the degree of inhibition in viral growth imposed by endosomal restriction factors by
400 fitting our model to data where the cells were treated with Amphotericin B, as Amphotericin B inhibits
401 the action of endosomal restriction factors. The main hypotheses tested were i) whether Omicron
402 was able to evade endosomal restriction in hNECs; ii) whether this evasion enabled Omicron to use
403 TMPRSS2-independent pathways; and iii) whether this was responsible for Omicron's growth
404 advantage. We found that the fitness of Delta in hNECs without endosomal restriction, as measured
405 by the basic reproduction number $R_{0X}$ and the growth rate $r_X$, was still lower than that of Omicron in
406 hNECs with endosomal restriction. Hence, reduced endosomal restriction alone do not explain
407 Omicron's fitness advantage in hNECs. Although we were able to quantify the degree of inhibition by
408 endosomal restriction factors for both pathways for Omicron in hNECs, we were unable to do so for
409 Delta, as doing so requires either the infectious viral load to be above the limit of detection in the
410 presence of Camostat (as was the case for Omicron in hNECs), or requires data on viral growth in the
411 presence of both drugs (as was the case in Calu-3 cells). Hence, we were unable to make a direct
412 comparison at a pathway-specific level between Omicron and Delta in hNECs. In Calu-3 cells, we found
413 that Omicron was more inhibited by endosomal restriction factors than Delta, for either TMPRSS2-
414 dependent or TMPRSS2-independent pathways.

415 The model has several limitations. First, we fixed the infected cell death rate, the rate at which viruses
416 lose infectivity, the RNA degradation rate and the duration of eclipse phases, according to values from
417 the literature. It is currently unclear whether the duration of the eclipse phase differs between
418 variants. To test this, we conducted a sensitivity analysis where the model was fitted assuming
419 different lengths of the eclipse phase. This sensitivity analysis showed that if eclipse phase lengths
420 were assumed to be the same between Omicron and Delta, while the estimated values of $R_0$ changed
421 with the assumed length of the eclipse phase, the trends and relationships in $R_0$ and the growth rate
422 estimates $r$ between Omicron and Delta (for example, that Omicron has a higher $R_0$ and growth rate
423 estimate $r$ than Delta in hNECs) remained unchanged. Allowing the eclipse phase to be different
424 between strains, no longer allows us to draw conclusions about whether $R_0$ is greater for Omicron or
425 Delta (Supplementary Tables 3 and 5), but the differences in $r$ are robust. This result reflects the
426 finding that if the eclipse phase is allowed to vary, the growth rate $r$ is identifiable but $R_0$ is not. Future
427 studies could measure the duration of the eclipse phase for each cell type and virus strain using single-
428 cycle growth kinetics experiments.

429 We also did not test the effect of changing the assumed values of the infected cell or virus decay rates.
430 Studies have shown that Omicron survives for longer on surfaces than the ancestral strain[48] and
431 Delta[49], so it is plausible that extracellular virus may also differ in stability in our experiments.

432 Moreover, fixing the parameters using values from previous studies may underestimate the
433 uncertainty in $R_0$and r.

434 Another limitation of the model is that it assumes 100% effectiveness for both drugs. Assuming 100%
435 effectiveness of Camostat means interpreting all remaining viral growth as due to TMPRSS2-
436 independent pathways, so if the drug is less than 100% effective, the contribution of TMPRSS2-
437 independent pathways will be overestimated. Assuming 100% effectiveness of Amphotericin B means
438 interpreting viral growth in the presence of Amphotericin B as the viral growth in the complete
439 absence of endosomal restriction. If the drug were less than 100% effective, the viral load in the
440 complete absence of endosomal restriction could be higher than that suggested by the data, so the
441 effect of endosomal restriction would be underestimated.

442 Last, the structure of the model is such that the initial growth rate is independent of the inoculum
443 size. It is plausible that differences in growth rate between hNECs and Calu-3 cells observed in the
444 experiments were partly due to the differing inoculum sizes used, as a higher inoculum could, for
445 example, trigger endosomal restriction factors more quickly – an effect which was not modelled. A
446 higher multiplicity of infection (MOI) was used for hNECs as a lower MOI did not always successfully
447 infect these primary cells; repeating the Calu-3 experiments at the same higher MOI would strengthen
448 confidence in our comparison between cell types.

449 The models developed in this study can inform future studies using more complex models. Models
450 capturing more immune components and how the virus spreads within the host are useful for
451 understanding contributors to disease severity and the effects of antivirals[32–34], but because they have
452 many parameters, it is often difficult to determine their values by fitting them to data. This study can
453 help parameterize these models.

454 The models developed in this study can be applied to different SARS-CoV-2 virus strains to help
455 enhance our understanding of transmission potential of new strains as the virus continues to evolve.
456 While between-strain differences in the speed of viral replication is typically assessed by comparing
457 viral titre measurements at individual timepoints, adopting a mathematical modelling approach using
458 longitudinal timepoints enables us to estimate key characteristics of different strains such as the
459 growth rate and viral fitness, thus providing a deeper insight into the factors shaping observed
460 differences in viral dynamics at the individual and population level.

461

462 ## References


463 1. WHO. Classification of Omicron (B.1.1.529): SARS-CoV-2 Variant of Concern. *Who* 1
464 https://www.who.int/news/item/26-11-2021-classification-of-omicron-(b.1.1.529)-sars-cov-
465 2-variant-of-concern (2021).

466 2. GISAID. GISAID - hCov19 Variants. *Gisaid* https://gisaid.org/hcov19-variants/ (2022).

467 3. WHO. Tracking SARS-CoV-2 variants. *Who* https://www.who.int/en/activities/tracking-SARS-
468 Co Preprint at (2021).

469 4. Viana, R. *et al.* Rapid epidemic expansion of the SARS-CoV-2 Omicron variant in southern
470 Africa. *Nature* **603**, 679–686 (2022).

471 5. Cele, S. *et al.* Omicron extensively but incompletely escapes Pfizer BNT162b2 neutralization.
472 *Nature* **602**, 654–656 (2022).

473 6. Planas, D. *et al.* Considerable escape of SARS-CoV-2 Omicron to antibody neutralization.
474 *Nature* **602**, 671–675 (2022).

475 7. Cao, Y. *et al.* Omicron escapes the majority of existing SARS-CoV-2 neutralizing antibodies.
476 *Nature* **602**, 657–663 (2022).

477 8. Dejnirattisai, W. *et al.* SARS-CoV-2 Omicron-B.1.1.529 leads to widespread escape from
478 neutralizing antibody responses. *Cell* **185**, 467-484.e15 (2022).

479 9. Andrews, N. *et al.* Covid-19 Vaccine Effectiveness against the Omicron (B.1.1.529) Variant.
480 *New England Journal of Medicine* **386**, 1532–1546 (2022).

481 10. Nyberg, T. *et al.* Comparative analysis of the risks of hospitalisation and death associated with
482 SARS-CoV-2 omicron (B.1.1.529) and delta (B.1.617.2) variants in England: a cohort study. *The*
483 *Lancet* **399**, 1303–1312 (2022).

484 11. Wolter, N. *et al.* Early assessment of the clinical severity of the SARS-CoV-2 omicron variant in
485 South Africa: a data linkage study. *The Lancet* **399**, 437–446 (2022).

486 12. Hui, K. P. Y. Y. *et al.* SARS-CoV-2 Omicron variant replication in human bronchus and lung ex
487 vivo. **603**, (2022).

488 13. Willett, B. J. *et al.* SARS-CoV-2 Omicron is an immune escape variant with an altered cell entry
489 pathway. *Nature Microbiology 2022 7:8* **7**, 1161–1179 (2022).

490 14. Barut, G. T. *et al.* The spike gene is a major determinant for the SARS-CoV-2 Omicron-BA.1
491 phenotype. *Nat Commun* **13**, 1–14 (2022).

492 15. Lyngse, F. P. *et al.* Household transmission of the SARS-CoV-2 Omicron variant in Denmark.
493 *Nat Commun* **13**, 5573 (2022).

494 16. Willett, B. J. *et al.* SARS-CoV-2 Omicron is an immune escape variant with an altered cell entry
495 pathway. *Nat Microbiol* (2022) doi:10.1038/s41564-022-01143-7.

496 17. Meng, B. *et al.* Altered TMPRSS2 usage by SARS-CoV-2 Omicron impacts infectivity and
497 fusogenicity. *Nature 2022 603:7902* **603**, 706–714 (2022).

498 18. Suzuki, R. *et al.* Attenuated fusogenicity and pathogenicity of SARS-CoV-2 Omicron variant.
499 *Nature* **603**, 700–705 (2022).

500 19. Hoffmann, M. *et al.* SARS-CoV-2 Cell Entry Depends on ACE2 and TMPRSS2 and Is Blocked by
501 a Clinically Proven Protease Inhibitor. *Cell* **181**, 271-280.e8 (2020).

502 20. Peacock, T. P. *et al.* The altered entry pathway and antigenic distance of the SARS-CoV-2
503 Omicron variant map to separate domains of spike protein. *bioRxiv* 2021.12.31.474653 (2022)
504 doi:10.1101/2021.12.31.474653.

505 21. Winstone, H. *et al.* The Polybasic Cleavage Site in SARS-CoV-2 Spike Modulates Viral
506 Sensitivity to Type I Interferon and IFITM2. *J Virol* **95**, e02422-20 (2021).

507 22. Peacock, T. P. *et al.* The furin cleavage site in the SARS-CoV-2 spike protein is required for
508 transmission in ferrets. *Nat Microbiol* **6**, 899–909 (2021).

509 23. Khan, H. *et al.* TMPRSS2 promotes SARS-CoV-2 evasion from NCOA7-mediated restriction.
510 *PLoS Pathog* **17**, e1009820 (2021).

511 24. Challenger, J. D. *et al.* Modelling upper respiratory viral load dynamics of SARS-CoV-2. *BMC*
512 *Med* **20**, 25 (2022).

513 25. Ke, R., Zitzmann, C., Ho, D. D., Ribeiro, R. M. & Perelson, A. S. In vivo kinetics of SARS-CoV-2
514 infection and its relationship with a person's infectiousness. *Proc Natl Acad Sci U S A* **118**,
515 e2111477118 (2021).

516 26. Gonçalves, A. *et al.* Timing of Antiviral Treatment Initiation is Critical to Reduce SARS-CoV-2
517 Viral Load. *CPT Pharmacometrics Syst Pharmacol* **9**, 509–514 (2020).

518 27. Gonçalves, A. *et al.* SARS-CoV-2 viral dynamics in non-human primates. *PLoS Comput Biol* **17**,
519 (2021).

520 28. Perelson, A. S. & Ke, R. Mechanistic Modeling of SARS-CoV-2 and Other Infectious Diseases
521 and the Effects of Therapeutics. *Clin Pharmacol Ther* **109**, 829–840 (2021).

522 29. Koelle, K. *et al.* Masks Do No More Than Prevent Transmission: Theory and Data Undermine
523 the Variolation Hypothesis. Preprint at https://doi.org/10.1101/2022.06.28.22277028 (2022).

524 30. Ito, K., Piantham, C. & Nishiura, H. Relative instantaneous reproduction number of Omicron
525 SARS-CoV-2 variant with respect to the Delta variant in Denmark. *J Med Virol* **94**, 2265–2268
526 (2022).

527 31. Alexandre, M. *et al.* Modelling the response to vaccine in non-human primates to define
528 SARS-CoV-2 mechanistic correlates of protection. *Elife* **11**, e75427 (2022).

529 32. Jenner, A. L. *et al.* COVID-19 virtual patient cohort suggests immune mechanisms driving
530 disease outcomes. *PLoS Pathog* **17**, e1009753 (2021).

531 33. Rowlatt, C. F. *et al.* Modelling the within-host spread of SARS-CoV-2 infection, and the
532 subsequent immune response, using a hybrid, multiscale, individual-based model. Part I:
533 Macrophages. *bioRxiv* (2022) doi:10.1101/2022.05.06.490883.

534 34. Getz, M. *et al.* Iterative community-driven development of a SARS-CoV-2 tissue simulator.
535 *bioRxiv* (2021) doi:10.1101/2020.04.02.019075.

536 35. Marc, A. *et al.* Quantifying the relationship between SARS-CoV-2 viral load and infectiousness.
537 *Elife* **10**, e69302 (2021).

538 36. Larremore, D. B. *et al.* Test sensitivity is secondary to frequency and turnaround time for
539 COVID-19 screening. *Sci Adv* **7**, eabd5393 (2021).

540 37. Hay, J. A. *et al.* Estimating epidemiologic dynamics from cross-sectional viral load
541 distributions. *Science (1979)* **373**, eabh0635 (2021).

542 38. Brass, A. L. *et al.* The IFITM Proteins Mediate Cellular Resistance to Influenza A H1N1 Virus,
543 West Nile Virus, and Dengue Virus. *Cell* **139**, 1243–1254 (2009).

544 39. Lin, T.-Y. *et al.* Amphotericin B Increases Influenza A Virus Infection by Preventing IFITM3-
545 Mediated Restriction. *Cell Rep* **5**, 895–908 (2013).

546 40. Qian, J. *et al.* Primate lentiviruses are differentially inhibited by interferon-induced
547 transmembrane proteins. *Virology* **474**, 10–18 (2015).

548 41. Brahim Belhaouari, D. *et al.* The Strengths of Scanning Electron Microscopy in Deciphering
549 SARS-CoV-2 Infectious Cycle. *Front Microbiol* **11**, 2014 (2020).

550 42. Hou, Y. J. *et al.* SARS-CoV-2 D614G variant exhibits efficient replication ex vivo and
551 transmission in vivo. *Science (1979)* **370**, 1464–1468 (2020).

552 43. Shuai, H. *et al.* Attenuated replication and pathogenicity of SARS-CoV-2 B.1.1.529 Omicron.
553 *Nature* **603**, 693–699 (2022).

554 44. Cameroni, E. *et al.* Broadly neutralizing antibodies overcome SARS-CoV-2 Omicron antigenic
555 shift. *Nature* **602**, 664–670 (2022).

556 45. Mannar, D. *et al.* SARS-CoV-2 Omicron variant: Antibody evasion and cryo-EM structure of
557 spike protein–ACE2 complex. *Science (1979)* **375**, 760–764 (2022).

558 46. Zhang, J. *et al.* Structural and functional impact by SARS-CoV-2 Omicron spike mutations. *Cell*
559 *Rep* **39**, 110729 (2022).

560 47. Metzdorf, K. *et al.* TMPRSS2 Is Essential for SARS-CoV-2 Beta and Omicron Infection. *Viruses*
561 **15**, 271 (2023).

562 48. Chin, A. W. H., Lai, A. M. Y., Peiris, M. & Man Poon, L. L. Increased Stability of SARS-CoV-2
563 Omicron Variant over Ancestral Strain. *Emerging Infectious Disease journal* **28**, 1515 (2022).

564 49. Hirose, R. *et al.* Differences in environmental stability among SARS-CoV-2 variants of concern:
565 Both Omicron BA.1 and BA.2 have higher stability. *Clinical Microbiology and Infection* (2022)
566 doi:https://doi.org/10.1016/j.cmi.2022.05.020.

567

568 # Acknowledgements

569 CMC and ID acknowledge funding from the MRC Centre for Global Infectious Disease Analysis
570 (reference MR/R015600/1), jointly funded by the UK Medical Research Council (MRC) and the UK
571 Foreign, Commonwealth & Development Office (FCDO), under the MRC/FCDO Concordat agreement
572 and is also part of the EDCTP2 programme supported by the European Union. AWCY acknowledges
573 funding from an Imperial College Research Fellowship. ID acknowledges funding by the Wellcome

Trust and Royal Society (grant number 213494/Z/18/Z). This study was conducted as part of G2P-UK National Virology consortium funded by MRC/UKRI (MR/W005611/1). For the purpose of open access, the authors have applied a CC BY public copyright licence to any Author Accepted Manuscript version arising from this submission.

## Author Contributions

CMC, AWCY, WSB and ID conceived the study; JCB and KS generated the *in-vitro* data; CMC, AWCY and ID conceived the mathematical models; CMC performed the analysis for Model 1; AWCY performed the analysis for Model 2; CMC, AWCY, JCB, TPP, WSB, and ID contributed to the interpretation of the results; CMC and AWCY wrote the first draft of the manuscript; all authors reviewed and approved the final version of the manuscript.

## Competing Interests

The authors declare no competing financial interests.